

Assessing the capabilities of high-resolution spectral, altimetric, and textural descriptors for mapping the status of citrus parcels

Sergio Morell-Monzó^a, Javier Estornell^b, María-Teresa Sebastiá-Frasquet^c

^a Universitat Politècnica de Valencia. EPS Gandia, C/ Paraninfo, 1, 46730 Gandia, Spain

^b Geo-Environmental Cartography and Remote Sensing Group, Universitat Politècnica de Valencia, Camí de Vera s/n, 46022 Valencia, Spain

^c Instituto de Investigación para la Gestión Integrada de Zonas Costeras, Universitat Politècnica de Valencia, C/ Paraninfo, 1, 46730 Grau de Gandia, Spain



ARTICLE INFO

Keywords:

Agricultural land abandonment
Citrus crops
Worldview-3
Airborne imagery
Structure
From motion point clouds

ABSTRACT

Agricultural land abandonment is an increasing phenomenon around the world with relevant environmental and socio-economic implications. In the European Union about 11 % of agricultural land is at high risk of abandonment. The Comunitat Valenciana region (Spain) is the most important citrus producer in Europe suffering from this problem. Identifying the status of citrus crops at the parcel level is essential for policymakers in agriculture. This work assessed the use of WorldView-3 data, Very High-Resolution Airborne Images, and Structure from Motion point clouds to identify the status of citrus parcels using two machine learning algorithms: Random Forest and Support Vector Machines. Different analyses involving combinations of the three data sources were carried out to assess the impact on classification accuracy. The results showed the high potential of airborne imagery ($OA \approx 0.967$) and WorldView-3 ($OA \approx 0.936$) to detect parcel status using a single image. The SfM data showed a lower potential ($OA \approx 0.825$). Adding SfM point cloud to the multispectral information produced small improvements (0.4–2.0 %) in classification accuracy. The class separability analysis showed the importance of WV-3 SWIR bands to detect abandoned parcels as they produce more spectral separability over the productive parcels in the 1570 nm – 2330 nm spectrum. The results also show the importance of GLCM texture features extracted from sub-metric images due to their ability to model spatial planting patterns typical of fruit crops.

1. Introduction

Agricultural land abandonment (ALA) is an increasing issue around the world with relevant environmental (e.g., biodiversity, carbon sequestration, novel ecosystems, wildfires, and water resources) and socio-economic (e.g., food production, livelihood, and landscape) implications (Prishchepov, 2020). This issue occurs in variable social, environmental, and economic contexts (Kosmas et al. 2015). However, it is particularly prevalent in mountainous zones and in areas with highly fragmented parcel structures (Czesak et al. 2021). Depending on the type of crop, the social, and environmental context, ALA can be perceived as a problem or as an opportunity since it can have negative and positive effects on the environment and society (Subedi et al. 2021). These characteristics make ALA a complex phenomenon that must be studied at different scales (global, regional, and local) (Strijker, 2005). In the European Union about 11 % of agricultural land is at high risk of abandonment (Perpiñá-Castillo et al. 2018). Therefore, time and cost-effective methods are urgently needed to identify ALA to provide land

managers and policymakers with information on land use changes and to continuously update the European Common Agricultural Policy.

The Comunitat Valenciana (CV) region (Eastern Spain) is the most important citrus producer in Europe. It produces more than 3 million Tn of mandarins and oranges annually (50 % and 45 % of Spain's citrus industry, respectively) (IVIA, 2022). In 2021, the area dedicated to citrus was estimated at 160,088 ha (MAPA, 2021). However, from 2000 to 2020 there has been a decrease of around 20 % of the area dedicated to citrus crops (MAPA, 2022). Identifying the status of citrus crops at the parcel level with high accuracy is essential for the public administration to make decisions on agricultural policy and to supervise the payment of subsidies to farmers. This temporal and spatial-explicit information on ALA may help customize policy instruments for counteracting or reversing this process and to implement tailored monitoring and management measures of the landscape (Volpi et al., 2023).

In 2018, the European Commission approved the use of alternative methodologies to in situ verification for crop monitoring based on Earth Observation data (regulation No. 746/2018). First efforts on detecting

E-mail address: sermonon@upv.es (S. Morell-Monzó).

ALA via Earth Observation data focused on the use of Landsat (e.g., Yin et al., 2018, Grădinaru, et al., 2019, Prishchepov, et al., 2012) and MODIS (e.g., Löw et al., 2018, Alcántara, et al., 2012, Estel et al., 2012) data. These studies focused on the use of time series of low and moderate-resolution imagery to detect ALA in seasonal crops and large areas that do not require high spatial resolution. More recent studies show that the higher spatial resolution of Sentinel-2 imagery made possible to address the ALA issue (e.g., Szostak et al., 2017, Volpi et al., 2023). These new capabilities motivated some authors to use these images to identify ALA at patch-level and pixel-level (Ruiz et al., 2020, Portalès-Julià, et. al., 2021). There are also experiences on the use of 3D data for the detection of ALA. The works of Kolecka et al. (2015) and Czesak et al. (2021) used LiDAR data to map the abandonment of seasonal crops. LiDAR data allowed to detect of advanced stages of ALA and secondary forest successions in areas with highly fragmented landscapes that were once occupied by crops.

Despite the advances, the operational implementation of citrus crop monitoring is still challenging in highly fragmented landscapes. These are common in the CV, where the size of the parcels can be a limiting factor to apply Sentinel-2 imagery. Fragmented landscapes are also common in many European areas and some authors have studied the applicability limits of Sentinel-2 but for monitoring seasonal crops with higher spectral-temporal separability (Vajsová et. al., 2020). Also, in citrus crops parcels in production and abandoned have a very similar spectral response. In addition, unlike seasonal crops, citrus is a perennial crop that does not have a cycle throughout the year (e.g., wrought, planting, germination, growth, and harvest) which could help to distinguish them from abandoned fields. The VHSR data can produce better results because its sub-metric resolution can capture textures caused by planting patterns (also called planting frames) characteristic of fruit crops, which is not possible with Sentinel-2 10 m resolution. Furthermore, 3D point clouds can provide new information that can improve the identification of citrus crops' status. Several studies have combined aerial and satellite imagery with 3D point clouds to improve crop type and other land cover classifications (Prins & Van Niekerk,

2021).

The objective of this paper is to evaluate the use of three VHSR data sources to identify the status of citrus crops: WorldView-3 (WV-3) imagery including visible and near-infrared (VNIR) and short-wave infrared (SWIR) bands, Very High-Resolution Airborne (VHRA) imagery, and 3D point clouds generated applying Structure from Motion (SfM) on images captured by a Remotely Piloted Aircraft System – RPAS. The classification performance including texture features for each data type is also analyzed. Additionally, the study evaluates the fusion of multi-spectral data and 3D point clouds to identify citrus crops' status. Two algorithms widely used in land cover classification problems are compared: Random Forest (RF) and Support Vector Machines (SVM). Finally, the relevance of the descriptors used for the classification and the class separability is statistically analyzed.

2. Materials and methods

2.1. Study area

The study area is located in the CV region (Eastern Spain) (Fig. 1), between the coastal municipalities of Gandia and Oliva ($38^{\circ}56'14.14''N$, $0^{\circ}8'42.03''W$), which occupies around 10,000 ha. In this area various land uses coexist such as urban, forestry, and agricultural use. The majority crop in this zone is citrus which occupies more than 95 % of the agricultural area (Generalitat Valenciana, 2021). The agricultural area is located on the coastal plain which is characterized by its flat relief, soils with high agronomic capacity, and availability of water. These characteristics have made this region a historically agricultural area. In recent years there has been a general abandonment of citrus. The agricultural structure is characterized by the small size of parcels (average 0.20–0.40 ha) and the high fragmentation of the landscape.

2.2. Spatial data and feature extraction

World View-3 images with values of top-of-atmosphere radiance

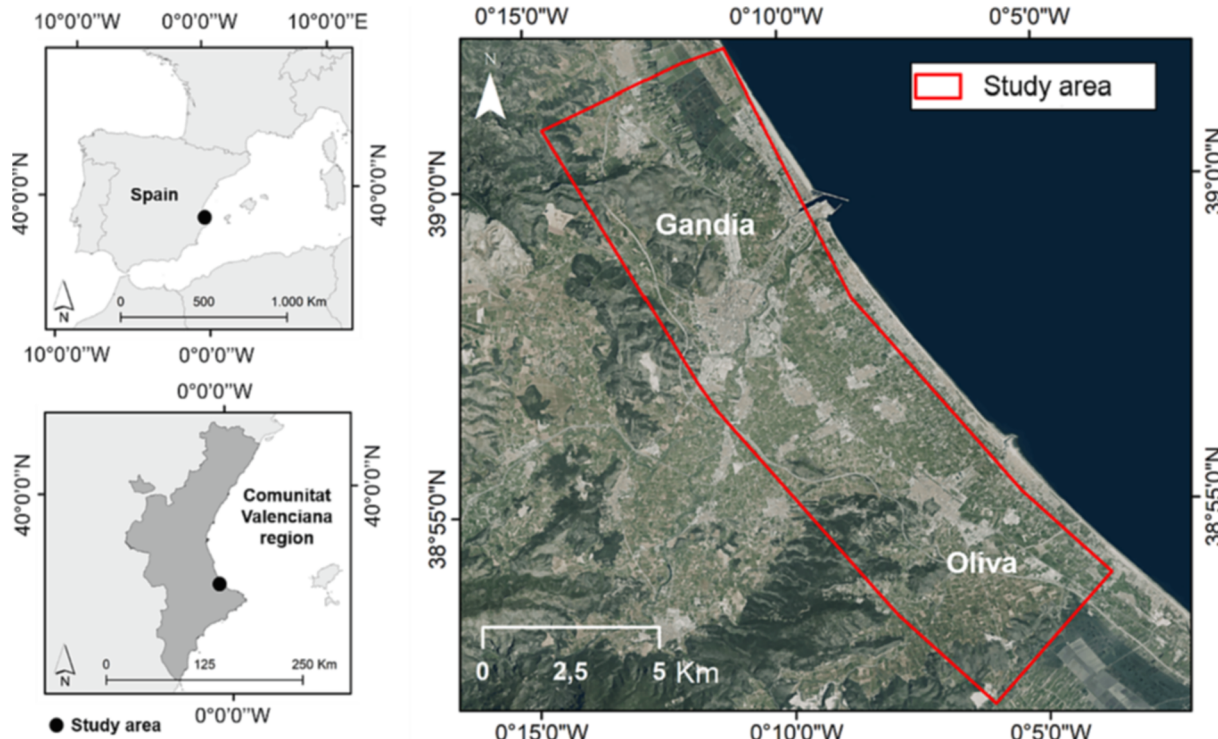


Fig. 1. Study area between the municipalities of Gandia and Oliva in the Comunitat Valenciana region (eastern Spain). Centre of the image: $38^{\circ}56'14.14''N$, $0^{\circ}8'42.03''W$.

were acquired on November 11, 2020. The acquired WV-3 image contains 8 VNIR bands (Coastal blue 425 nm, Blue 480 nm, Green 545 nm, Yellow 605 nm, Red 660 nm, Red-edge 725 nm, NIR1 835 nm, and NIR2 950 nm) of 11-bits and 2 m resolution, one pan-chromatic band (450–800 nm) of 11-bits and 0.5 m resolution, and 8 SWIR bands (SWIR1 1210 nm, SWIR2 1570 nm, SWIR3 1660 nm, SWIR4 1730 nm, SWIR5 2165 nm, SWIR6 2205 nm, SWIR7 2260 nm, SWIR8 2330 nm) of 14-bits and 3.7 m resolution (Digital Globe, 2014). The WV-3 product was orthorectified and atmospherically corrected using the ATCOR2 algorithm (Richter & Schläpfer, 2019a; Richter & Schläpfer, 2019b) to obtain surface reflectance images. To combine images with different spatial resolutions resampling processes were applied. The panchromatic band with a resolution of 0.5 m was resampled at a resolution of 1 m. The average was used as the aggregating criteria of the pixels. Then the VNIR (2 m) and SWIR (3.7 m) bands were resampled to 1 m using the nearest neighbor and de panchromatic band as reference.

To produce new descriptors for the classifier, 7 texture features were computed from the panchromatic band. The texture is an important characteristic of images that informs about the spatial distribution of the different pixel intensity levels. This spatial information is not necessarily correlated with spectral data, so including texture descriptors could improve classification accuracy (Hall-Beyer, 2017). In this study, the Gray Level Co-Occurrence Matrix (GLCM) method (Haralick et al., 1973) was used to compute texture features. These were calculated from 64 gray levels in an invariant direction that is the average of the four directions: 0°, 45°, 90°, and 135°. This omnidirectional approach was chosen due to planting frames do not present a specific direction. Two first-order histogram texture features were calculated: mean, variance, and five GLCM texture features: entropy, contrast, dissimilarity, angular second moment (ASM), and homogeneity (Morell-Monzo et al., 2021).

Very High-Resolution Airborne (VHRA) Imagery was also used in this study. This data was provided by the Valencian Cartographic Institute (ICV) (Source: <https://idev.gva.es/va> Orthophoto 2020 CC BY 4.0 © Institut Cartogràfic Valencià, Generalitat Valenciana). These images were taken on a photogrammetric flight on May 6, 2020 with an UltraCam Eagle UC-E-1-50016095-f80 camera from the company Vexcel Imaging GmbH © with a Qioptic Vexcel HR Digaron sensor. The ICV provides an annual VHRA image of the entire Valencian Region in tiles of 15160 × 10160 pixels. These images have a spatial resolution of 0.25 m and 4 spectral bands (Blue 430 nm, Green 530 nm, Red 620 nm, Red-edge 720 nm). These images were radiometrically calibrated and geometrically corrected ($\text{RMSE} < 4 \text{ cm}$) by Vexcel Imaging GmbH ©. 11 tiles were processed and resampled to 1 m to reduce the computational requirements and the pixels' spectral variability within each parcel. The value of the resampled pixels was based on the average value of the aggregated pixels. Finally, the same 7 texture features were computed from the Normalized Difference Vegetation Index (NDVI). The NDVI was computed by the normalized difference of the Red and Red-edge bands.

A photogrammetric point cloud was obtained through 12 RPAS flights carried out in February 2021. The RPAS was a senseFly eBee X which incorporates a S.O.D.A. RGB 20.1 MP and an RTK/PPK positioning system (3–8 cm positioning error). The flight height was around 123.7 m in nadir shots. A total of 5510 images were taken with 60 % lateral overlap and 80 % flight direction overlap. The images were processed using the SfM technique to obtain a 3D point cloud. No additional control points were required thanks to the RTK/PPK positioning system. An alignment error < 6 cm was obtained. Then a dense point cloud (325 points/m²) with approximately 4723 million points was generated. The dense point cloud was homogenized and its density was reduced to decrease processing time. Homogenization was performed at a target density of 50 points/m². The Progressive Morphological Filter (PMF) method (Zhang et al., 2003) was used to identify the ground points. It is well known that correctly identifying ground points from SfM point clouds can be a challenging task, especially in steeply sloping areas and dense vegetation. However, citrus crops in our study area have some characteristics that make this task easier. Citrus, which are irrigated crops, must necessarily be located in parcels with low slopes (<3%) to apply

irrigation properly. In addition, agricultural practices require spaces between tree rows and at the parcel boundaries. These spaces make that a significant set of ground points are retrieved correctly. On the other hand, farmers need to keep their parcels free of vegetation to facilitate agricultural practices, which helps to reduce DTM overestimation. In this context, the PMF algorithm, which is one of the standard methods, provided sufficiently accurate results. The Digital Terrain Model (DTM) with a cell size of 1 m × 1 m was computed. Then the Digital Surface Model (DSM) was computed using the pit-free method (Khosravipour et al., 2014). Finally, the Canopy Height Model (CHM) and 9 statistics were extracted from the normalized point cloud: mean H , standard deviation H , maximum H , minimum H , range of H , variance H , skewness H , kurtosis H , and entropy of H , where H is the height above the ground. These features were stored in a 1 m raster grid. Additionally, the same 7 texture features computed from the CHM were calculated and added to the raster grid to produce new descriptors for the classifier.

In order to generate useful information to detect, quantify and manage citrus crops abandonment, a classification was defined based on three types of parcels: non-productive (NP), productive (PR), and abandoned (AB) as shown in Fig. 2. Identify the AB parcels is useful for monitoring land abandonment. Furthermore, identify the NP and PR parcels allows making more accurate crop yield estimations. Citrus parcels were previously identified from the Land Parcel Identification System (LPIS) database of Spain known as Sistema de Información Geográfica de Parcelas Agrícolas (SIGPAC).

Ground truth data were obtained through field campaigns conducted in February and March 2021. A systematic sampling of the area covered with the three data sources (WV-3, VHRA, and RPAS-SfM) was carried out. Verification was done through photointerpretation of RPAS images and the ICV orthophotos due to the different data acquisition of ground truth data and remote sensing. A total of 280 parcels without changes during the period May 2020 - February 2021 were selected. This dataset contains 60 NP, 120 PR, and 100 AB parcels. This unbalanced dataset keeps the proportions of each category observed in the field.

2.3. Classification

The classification approach used in this study is based on that proposed in Morell-Monzo et al. (2021) adapted to each data source. The general workflow consists of the following steps: 1) preprocessing raw data; 2) feature extraction (altimetric features, texture features, and pixel values for each band); 3) model training (RF or SVM) using pixels as training samples; 4) semantic segmentation of the image to create a pixel-based classification; 5) apply majority voting to obtain a single classification value per parcel.

In this work two commonly employed classification algorithms were used, Random Forest (Breiman, 2001) and Support Vector Machines (Cortes & Vapnik, 1995). Although there is a growing trend towards the use of deep learning algorithms, RF and SVM are still benchmark algorithms for many remote sensing problems (Sheykhou et al., 2020). This is due to their good performance with small amounts of training data and ease of use for non-expert users as they require few hyperparameters to be adjusted, they use non-sequential training, they are quite robust against overfitting they are computationally less demanding and they have higher interpretability compared with deep learning (Sheykhou et al., 2020). In land cover classifications, RF and SVM are two of the most popular methods (Saini and Ghosh, 2018).

The RF algorithm was applied using the randomForest R package (Liaw and Wiener, 2002). RF requires adjusting two main hyperparameters: the number of trees ($n\text{tree}$) that make up the forest, and the number of variables randomly selected in each node split ($m\text{try}$). In this study, the $n\text{tree}$ was adjusted to 250 and $m\text{try}$ was adjusted to \sqrt{M} , where M is the number of input variables. The impurity is used to search the optimal threshold at each node of the tree. RF used the Gini Index as a measure of impurity.

The SVM algorithm was applied using the e1071 R package (Meyer



Fig. 2. Example of the three parcel types classified: non-productive (left), productive (center) and abandoned (right).

et al., 2021). A SVM with a radial basin function kernel was used. It has two hyperparameters to adjust: the regularization parameter (C) and kernel bandwidth (γ). In this study the constant of regularization C was fixed to 1 and γ was adjusted to $\frac{1}{M^p}$ where M is the number of input variables (data dimensionality). The tolerance of termination criterion was set by default in 0.001.

2.4. Accuracy assessment and validation

First, the optimal kernel size for extracting texture features was obtained. The following kernel sizes were evaluated: 3x3, 5x5, 7x7, 9x9, 11x11, 13x13, 15x15, 17x17, 19x19, 21x21, 23x23 and 25x25. The optimal kernel size was the one that maximized the overall accuracy (OA) based on the RF classifier.

Once the optimal kernel size was obtained, the performance of each data bundle and its respective combinations was evaluated using both RF and SVM. Each model was evaluated using a 4-folds cross-validation approach using random splits without replacement. In each iteration, 3/4 of the parcels were used for training and 1/4 for validation, ensuring a balanced dataset with the same number of parcels of each class by iteration. The following performance metrics were calculated: OA, Cohen's Kappa, precision (producer's accuracy by class), and recall (user's accuracy by class).

$$\text{OverallAccuracy} = \frac{\sum CM_{ii}}{N} \quad (1)$$

Cohen's Kappa can be generalized to the m classes,

$$\text{Cohen'sKappa} = \frac{N\sum_{i=1}^m CM_{ii} - \sum_{i=1}^m Ci_{corr} Ci_{pred}}{N^2 - \sum_{i=1}^m Ci_{corr} Ci_{pred}} \quad (2)$$

where N is the total number of samples, m is the number of classes, CM_{ii} the diagonal elements of the confusion matrix, and Ci_{corr} and Ci_{pred} are the correct and predicted labels of the class i respectively.

$$\text{Precision}_i = \frac{TP_i}{TP_i + FP_i} \quad (3)$$

$$\text{Recall}_i = \frac{TP_i}{TP_i + FN_i} \quad (4)$$

where TP_i are the true positives for the i class, FP_i are the false positives for the i class, and FN_i are the false negative for the i class.

A second validation step was performed. In this case a spatial cross-validation with 4 clusters was performed. This validation technique was applied to avoid an underestimation of the model error due to spatial correlation of the samples which is inherent to remote sensed data (Karasiak et al., 2021). Random cross-validation can lead to error underestimation when data are strongly aggregated (Wadoux et al., 2021; Stock, 2022), as in our case. In this validation step, only the performance of the most accurate data bundle from each data source was evaluated.

Fig. 3 shows the different splits used in random and spatial cross-validation. Spatial clusters were generated by k-Means clustering from the XY coordinates of the parcels. This procedure allows to generate spatial groups of parcels with the greatest distance between groups. However, no balanced data splits are generated.

2.5. Descriptors' relevance and class separability

To evaluate the relevance of each descriptor, the Jeffries-Matusita (JM) distance was used. JM distance measures the separability between a pair of probability distributions. This method does not inform about the influence of a descriptor on the model performance but it collects the intrinsic structure of the variables. Unlike methods based on permutation or impurity (such as RF feature importance measures), this is a statistical method not biased against collinearity and cardinality. In addition, JM distance allows knowing the separability between pairs of classes, which favors the interpretation of the problem. The JM distance takes the range $[0, \sqrt{2}]$ and is defined as:

$$J_{xy} = \sqrt{2(1 - e^{-B_{xy}})} \quad (5)$$

where B_{xy} is the multivariate Bhattacharyya distance,

$$B_{xy} = \frac{1}{8}(x - y)^t \left(\frac{\sum x + \sum y}{2} \right)^{-1} (x - y) + \frac{1}{2} \ln \left(\frac{\left| \frac{\sum x + \sum y}{2} \right|^2}{\left| \sum x \right|^{\frac{1}{2}} + \left| \sum y \right|^{\frac{1}{2}}} \right) \quad (6)$$

where x is the first spectral signature vector, y is the second spectral signature vector, $\sum x$ is the covariance matrix of x , and $\sum y$ is the covariance matrix of y .

3. Results

3.1. Kernel size analysis

The kernel size used to extract texture features influences the performance of the model. The optimal kernel size depends on the size and shape of the parcels as well as the spatial resolution of the image. The theoretical behavior is that as the kernel size increases, a higher OA of the pixel-based classification is obtained due to the reduction of salt-and-pepper noise. For this reason, the larger kernel, produce the smaller improvements in OA of the parcel-based classification when majority voting is applied. However, if the window size increases too much, a decrease in parcel-based OA can occur. This can be explained considering that a too large window can include pixels from other categories and adjacent parcels. So, the pixels at the edges of the parcels can be misclassified.

The analysis of the kernel size used to extract the texture features is shown below (Fig. 4). The optimal window size to compute texture

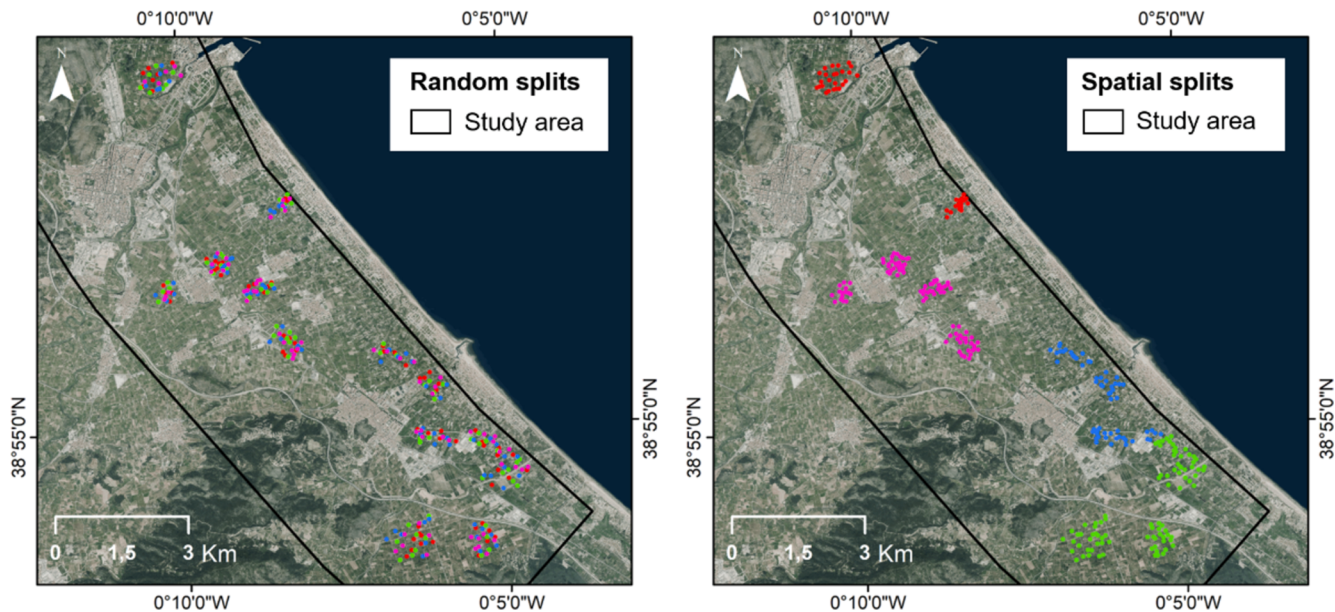


Fig. 3. Data splits used in random cross-validation (left) and spatial cross-validation (right).

features from the panchromatic band of WV-3 image was 7×7 . For the NDVI derived from the VHRA image was 11×11 . However, in this case the OA of the parcel-based classification remained stable for all window sizes (0.975–0.986). For the CHM derived from the SfM the optimal window size was 11×11 . For the SfM data, the OA of the parcel-based classification was even lower than the OA of the pixel-based classification (Fig. 3c) using a 25×25 kernel. On the other hand, the OOB error of the RF model decreased as the window size increased, so this measure is not recommended to adjust the kernel size as this will result in an underestimation of the error. This occurs because the OOB samples and the training samples are included in the same window. As the window size increase the OOB samples and the training samples are more correlated as they share more common neighbors.

3.2. Classification accuracy

The results of the random cross-validation for each data bundle are shown below (Fig. 5). The data source that produced the best results was the VHRA image (OA max = 0.986) followed by the WV-3 image (OA max = 0.954) and the SfM point cloud (OA max = 0.836). RF and SVM showed similar performance in VHRA image. But RF was slightly more accurate in the WV-3 images and SfM point clouds. Furthermore, RF is more convenient to larger datasets due to its lower time complexity. SVM has a time complexity $O(dn^2)$ or $O(dn^3)$ while RF has a time

complexity of $O(n \log(n) dk)$.

All the WV-3-based data bundles produced an OA between 0.882 and 0.954 (Table 1). The best performance was obtained using the VNIR bands, SWIR bands and GLCM texture features. This combination produced an OA of 0.954 using RF and 0.947 using SVM. Similar results were obtained by the VNIR bands and GLCM texture features with an OA of 0.954 using RF and 0.939 using SVM. Finally, the data bundle with the lowest performance was obtained when the VNIR bands were used only with an OA of 0.896 using RF and 0.882 using SVM.

Table 1 shows the performance by class of each WV-3 based data bundle. Adding GLCM texture features from the panchromatic band to VNIR multispectral data improved OA around 5.5 %. Adding texture features improved recall of NP class primarily. The texture features also improved the precision of the PR and AB classes and the recall of the AB class. Combinations which do not include texture features showed a larger commission error of the NP class due to the erroneous classification between PR and AB classes. Furthermore, the combinations incorporating VNIR bands without texture features generated a lower recall but higher precision for the NP class. In this case, the high commission error of the NP class was caused by the erroneous classification of the AB class and, to a lesser extent, of the PR class. Adding SWIR bands to the VNIR bands produced improvements in AB class detection (improving both precision and recall).. Finally, the model which includes all the data bundles (VNIR, SWIR, and GLCM features) obtained

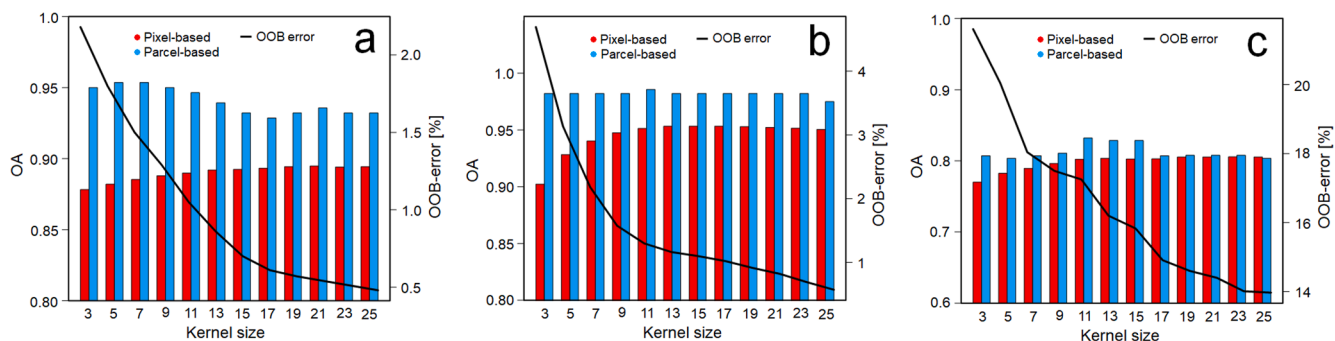


Fig. 4. Overall accuracy (OA) of the pixel-based classification (before majority voting step) and parcel-based (after majority voting step) and Random Forest's Out-Of-Bag error at each window size from 3×3 to 25×25 . a) corresponds to the WorldView-3 data, b) corresponds to the Very High-Resolution Airborne Imagery, and c) corresponds to the Structure from Motion data.

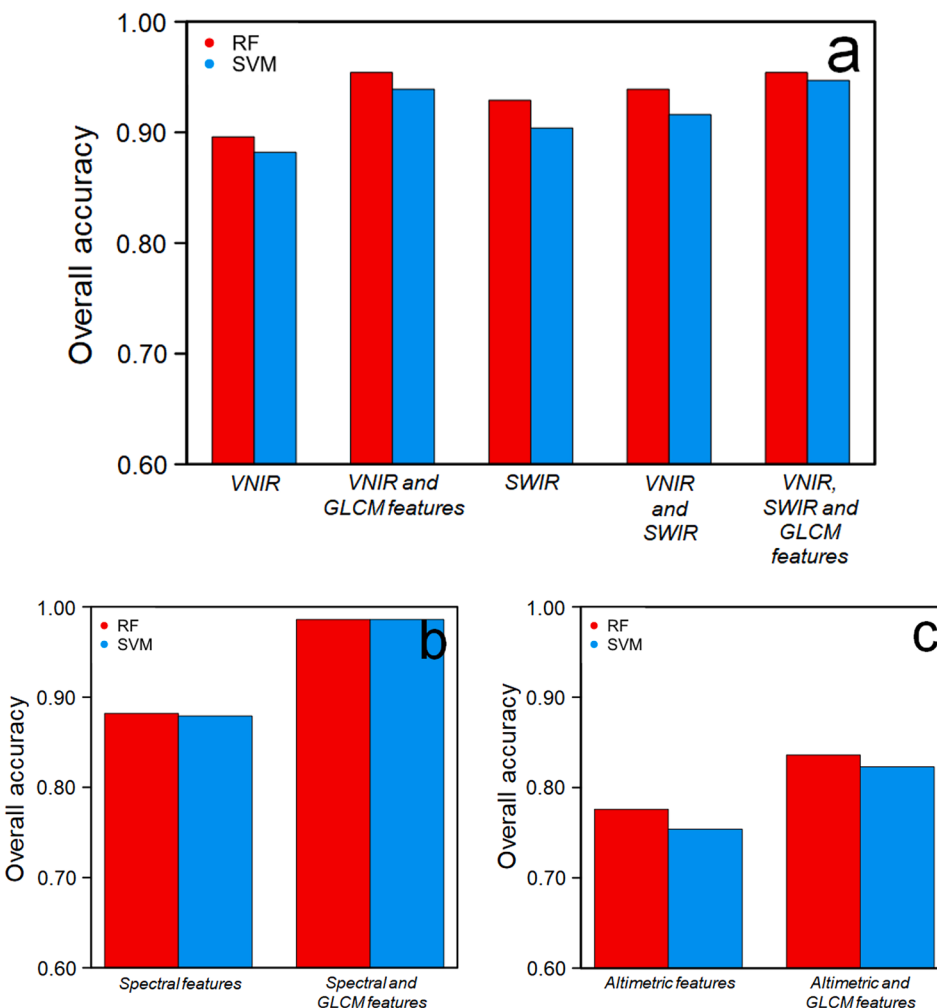


Fig. 5. Overall accuracy of the classification based on Random Forest (RF) and Support Vector Machines (SVM) for each data bundle: a) WorldView-3 subsets, b) Very High-Resolution Airborne Image subsets, and c) SfM point cloud subsets.

Table 1

Accuracy metrics of WorldView-3 based data bundles using random cross-validation. NP, PR and AB correspond to the non-productive, productive and abandoned parcels respectively.

	OA	Kappa	NP Precision	PR Precision	AB Precision	NP Recall	PR Recall	AB Recall
	(RF/ SVM)	(RF/ SVM)	(RF/ SVM)	(RF/ SVM)	(RF/ SVM)	(RF/ SVM)	(RF/ SVM)	(RF/ SVM)
VNIR bands	0.896 0.883	0.836 0.827	0.960 0.951	0.909 0.900	0.856 0.846	0.733 0.742	0.983 0.973	0.890 0.893
VNIR bands + GLCM features	0.954 0.939	0.927 0.915	0.948 0.951	0.959 0.949	0.931 0.908	0.900 0.867	0.975 0.974	0.940 0.965
SWIR bands	0.929 0.904	0.905 0.846	0.864 0.970	0.949 0.909	0.909 0.856	0.853 0.775	0.978 0.983	0.940 0.890
VNIR bands + SWIR bands	0.939 0.916	0.905 0.833	0.964 0.960	0.959 0.931	0.909 0.858	0.833 0.775	0.975 0.973	0.960 0.890
VNIR bands, SWIR bands + GLCM features	0.954 0.947	0.927 0.917	0.968 0.960	0.973 0.961	0.924 0.912	0.965 0.962	0.973 0.973	0.927 0.924

the best performance and showed a good balance between user's and producer's accuracy. According to this model, the most difficult class to detect was AB.

The VHRA image-based data bundles produced an OA between 0.882 and 0.986 (Table 2). The best performance was obtained using the VNIR bands and GLCM texture features derived from NDVI. This combination produced an OA of 0.986 using both RF and SVM. The data bundle that uses only the VNIR bands obtained a lower recall for the NP class but a

high precision. It produces a higher commission error for the NP class mainly due to the erroneous classification to PR class and AB class to a lesser extent. Adding texture features allowed to identify all the NP parcels correctly. Adding texture features also improved the precision and recall of the PR and AB classes, producing a good balance between precision and recall for all classes. Table 3..

The data bundles derived from SfM point cloud produced an OA between 0.754 and 0.836. The best performance was obtained using the

Table 2

Accuracy metrics of Very High-Resolution Airborne Imagery based data bundles using random cross-validation. NP, PR and AB correspond to the non-productive, productive and abandoned parcels respectively.

	OA	Kappa	NP Precision	PR Precision	AB Precision	NP Recall	PR Recall	AB Recall
	(RF/ SVM)	(RF/ SVM)	(RF/ SVM)	(RF/ SVM)	(RF/ SVM)	(RF/ SVM)	(RF/ SVM)	(RF/ SVM)
VNIR bands	0.882	0.814	1.000	0.806	0.944	0.867	0.958	0.800
	0.879	0.806	1.000	0.803	0.924	0.841	0.956	0.807
VNIR bands + GLCM features	0.986	0.978	1.000	0.992	0.971	1.000	0.975	0.990
	0.986	0.973	1.000	0.989	0.974	1.000	0.986	0.981

Table 3

Accuracy metrics of SfM point clouds-based data bundles using random cross-validation. NP, PR and AB correspond to the non-productive, productive and abandoned parcels respectively.

	OA	Kappa	NP Precision	PR Precision	AB Precision	NP Recall	PR Recall	AB Recall
	(RF/ SVM)	(RF/ SVM)	(RF/ SVM)	(RF/ SVM)	(RF/ SVM)	(RF/ SVM)	(RF/ SVM)	(RF/ SVM)
Altimetric features	0.776	0.568	0.827	0.758	0.692	0.627	0.851	0.840
	0.754	0.557	0.822	0.717	0.692	0.631	0.843	0.835
Altimetric + GLCM features	0.836	0.738	0.929	0.840	0.786	0.966	0.504	0.892
	0.823	0.738	0.909	0.831	0.788	0.960	0.528	0.863

3D point cloud features and the GLCM texture features derived from the CHM. This combination produced an OA of 0.8336 using RF and 0.823 using SVM. 3D data showed lower performance than the WV-3 and VHRAI. But these results show the potential of 3D point clouds data to monitor the status of citrus crops, specially including texture features derived from the CHM. Texture features improved the OA around 6.0 %.

The 3D point clouds and texture features allows to identify the NP class with high accuracy (0.929 of precision and 0.966 of recall using RF). However, these data showed low ability to separate the PR and AB parcels.

The results of the spatial cross-validation for the most accurate data bundle are shown below (Table 4). Spatial cross-validation show an average OA around 1.5 % lower than using the random cross-validation. These results suggest a small underestimation of the model error due to the spatial correlation of the parcels when using random cross-validation. Both RF and SVM were affected by this spatial correlation. In this case the most accurate data source was also the VHRA image (OA between 0.967–0.962) followed by the WV-3 image (OA between 0.936–0.935) and the SfM point cloud (OA = 0.822).

Fig. 6 shows the map of abandonment of citrus parcels in the study area. The map was generated by using the VHRA image and the Random Forest classifier. It can be seen that abandonment is concentrated mainly in coastal areas. In addition, there is a particularly high concentration of abandoned parcels near the protected wetlands of *Marjal de la Safor* (north of the map) and *Marjal Pego-Oliva* (south-east of the map). These results agree with our field work in the study area and our previous experiences (Morell-Monzo et al. 2021).

Table 4

Accuracy metrics for the best model of each data bundle. NP, PR and AB correspond to the non-productive, productive and abandoned parcels respectively using spatial cross-validation.

	OA	Kappa	NP Precision	PR Precision	AB Precision	NP Recall	PR Recall	AB Recall
	(RF/ SVM)	(RF/ SVM)	(RF/ SVM)	(RF/ SVM)	(RF/ SVM)	(RF/ SVM)	(RF/ SVM)	(RF/ SVM)
WV-3 (VNIR bands + SWIR bands + GLCM features)	0.936	0.907	0.917	0.960	0.914	0.961	0.958	0.911
	0.935	0.900	0.926	0.957	0.921	0.945	0.961	0.913
VHRAI (VNIR bands + GLCM features)	0.967	0.951	1.000	0.958	0.949	1.000	0.942	0.964
	0.962	0.948	1.000	0.967	0.930	1.000	0.939	0.945
SfM point cloud + GLCM features	0.822	0.714	0.914	0.838	0.776	0.957	0.618	0.878
	0.822	0.718	0.918	0.835	0.781	0.954	0.615	0.865

3.3. Spectral, altimetric, and textural combination

The performance obtained by combining spectral and 3D data is shown below (Table 5). The results indicate an improvement of 1.85 % in the OA when 3D point cloud features are added to the WV-3 images and an improvement of 0.55 % in the OA when these features are added to the VHRA image. The improvements produced by the 3D information were limited due to the good performance of the WV-3 images and the VHRA image, which have small margins of improvement.

3.4. Descriptors' relevance and class separability

Regarding the WV-3 descriptors, the bands in the visible spectrum (coastal blue, blue, green, yellow, red) produced a greater separability between the NP-AB classes, followed by NP-PR and PR-AB (Fig. 7a). In the near-infrared spectrum (red edge, NIR1, NIR2) the separability is minimized for all class combinations. The first order texture features, mean and variance, produced a similar separability to the visible bands due to its high correlation to the panchromatic band. However, the second order texture features improved the separability between the PR-AB classes, which are more difficult to separate. This explains the performance improvement produced by the texture features.

On the other hand, the SWIR bands produce a higher separability between the NP-AB classes, followed by PR-AB and NP-PR (Fig. 6b). This greater separability between the PR-AB classes explains the improvement in precision and recall of the AB class produced by the SWIR bands. There is a maximum separability of the PR-AB classes between 1570 nm and 2330 nm, which correspond to the SWIR2 and SWIR8 bands. In

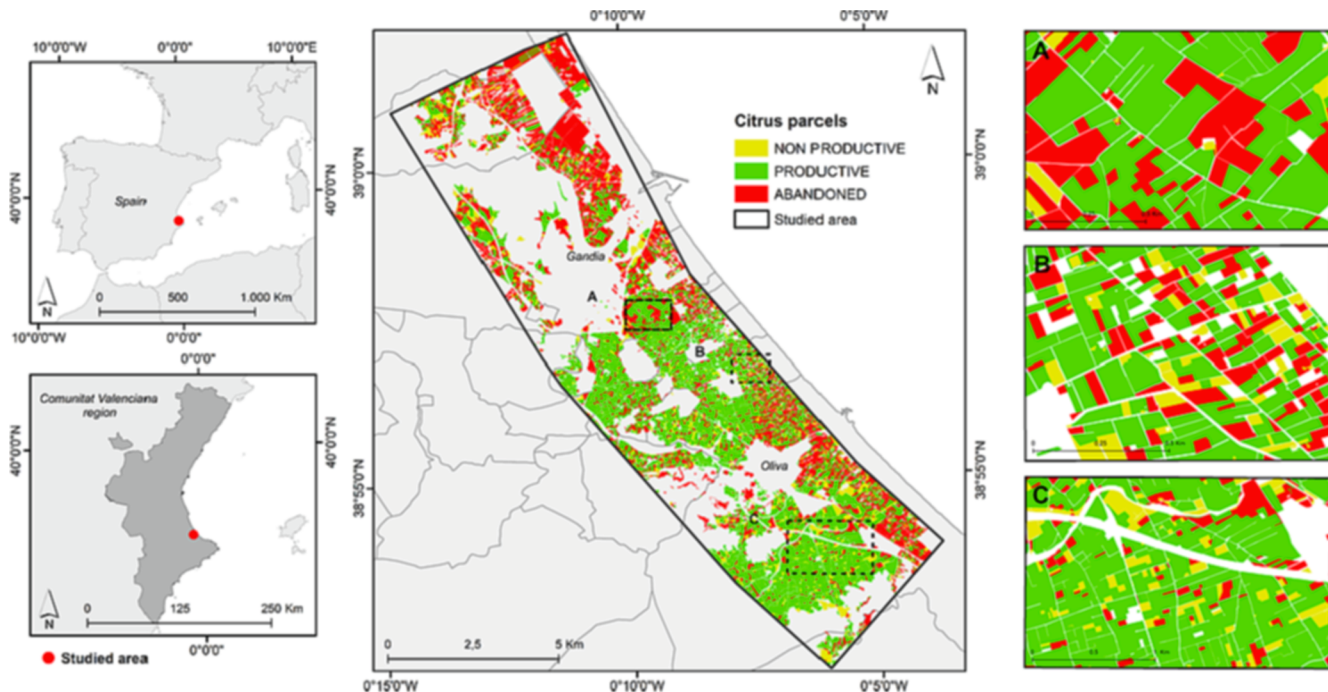


Fig. 6. Map of abandonment of citrus parcels between the municipalities of Gandia and Oliva in the Comunitat Valenciana region (Spain). The map was obtained using the Very High-Resolution Imagery of the Valencian Cartographic Institute of 2020 and the Random Forest classifier, which proved to be the most accurate results.

Table 5

Random Forest-based accuracy metrics obtained by combining spectral, 3D point cloud and textural descriptors. R-CV are the results obtained through random cross-validation and S-CV are the results obtained through spatial cross-validation. S + A is the accuracy metric obtained by combining spectral features, its texture features, 3D point cloud features, and its CHM texture features and Δ is the percentage of improvement produced by adding altimetric features to the spectral information. NP, PR and AB correspond to the non-productive, productive and abandoned parcels respectively.

	OA	Kappa	NP Precision	PR Precision	AB Precision	NP Recall	PR Recall	AB Recall
	(S + A/ $\Delta\%$)							
WV-3 + Altimetric features (R-CV)	0.971 +1.70	0.955 +2.80	1.000 +3.2	1.000 +2.70	0.931 +0.70	0.895 -7.00	1.000 +2.70	1.000 +7.30
WV-3 + Altimetric features (S-CV)	0.956 +2.00	0.927 +2.00	0.981 +6.4	0.968 +0.80	0.943 +2.90	0.972 +1.20	0.971 +1.30	0.902 -0.90
VHRAI + Altimetric features (R-CV)	0.993 +0.70	0.989 +1.10	1.000 +0.00	0.992 +0.00	0.990 +1.90	0.983 -1.70	1.000 +2.50	0.994 +0.40
VHRAI + Altimetric features (S-CV)	0.971 +0.40	0.961 +1.09	1.000 +0.00	0.968 +0.80	0.946 -0.30	1.000 +0.00	0.969 +2.90	0.950 -1.40

addition, there is a low separability in the SWIR1 band, which is the closest to the near-infrared spectrum.

Regarding the VHRA image-derived descriptors, the bands of the visible spectrum produced a greater separability between the NP-PR classes, followed by NP-AB and PR-AB (Fig. 7c). In this wavelength region, the separability between the NP-AB and PR-AB classes was similar to that of WV-3. However, the separability between the NP-PR classes was higher. The VHRA image also show a minimum of separability for all classes in the NIR - Red-edge wavelengths. On the other hand, texture features extracted from NDVI improved the separability between NP-AB and PR-AB classes. The results seem to indicate that extracting texture features from NDVI produce better results than from the WV-3 panchromatic band. This can be explained because NDVI produces a higher contrast between trees and bare soil.

Regarding the SfM point cloud descriptors, the highest separability occurred between the NP-AB classes (Fig. 7d). The combinations of NP-PR and PR-AB classes produced lower separability. Finally, texture features improved the separability of the PR-AB classes. These results show a certain potential of the texture features extracted from the CHM.

4. Discussion

This study evaluated the capabilities of high spatial resolution descriptors for mapping the status of citrus parcels in a highly fragmented agricultural system. The results show the potential of WV-3 imagery (including VNIR and SWIR bands), VHRA imagery with four VNIR bands, and SfM-derived point clouds to identify citrus crop status. Both WV-3 and VHRA imagery showed a high potential ($OA \geq 0.90$) to identify the crop status using a single image.

The WV-3 image achieved an OA between 0.954 and 0.935 using the VNIR band, SWIR bands, and GLCM texture features extracted from the panchromatic band. This image was taken in February where rainfall and higher soil moisture occur. Although farmers often control scrub, these conditions produce vegetation growth not associated with land abandonment that can affect imagery performance. The WV-3 SWIR bands showed a high potential specially to detect the abandoned parcels. The separability analysis showed that SWIR bands produce a higher separability between PR and AB crops, which are the most spectrally similar classes. These results can be explained as SWIR bands are related

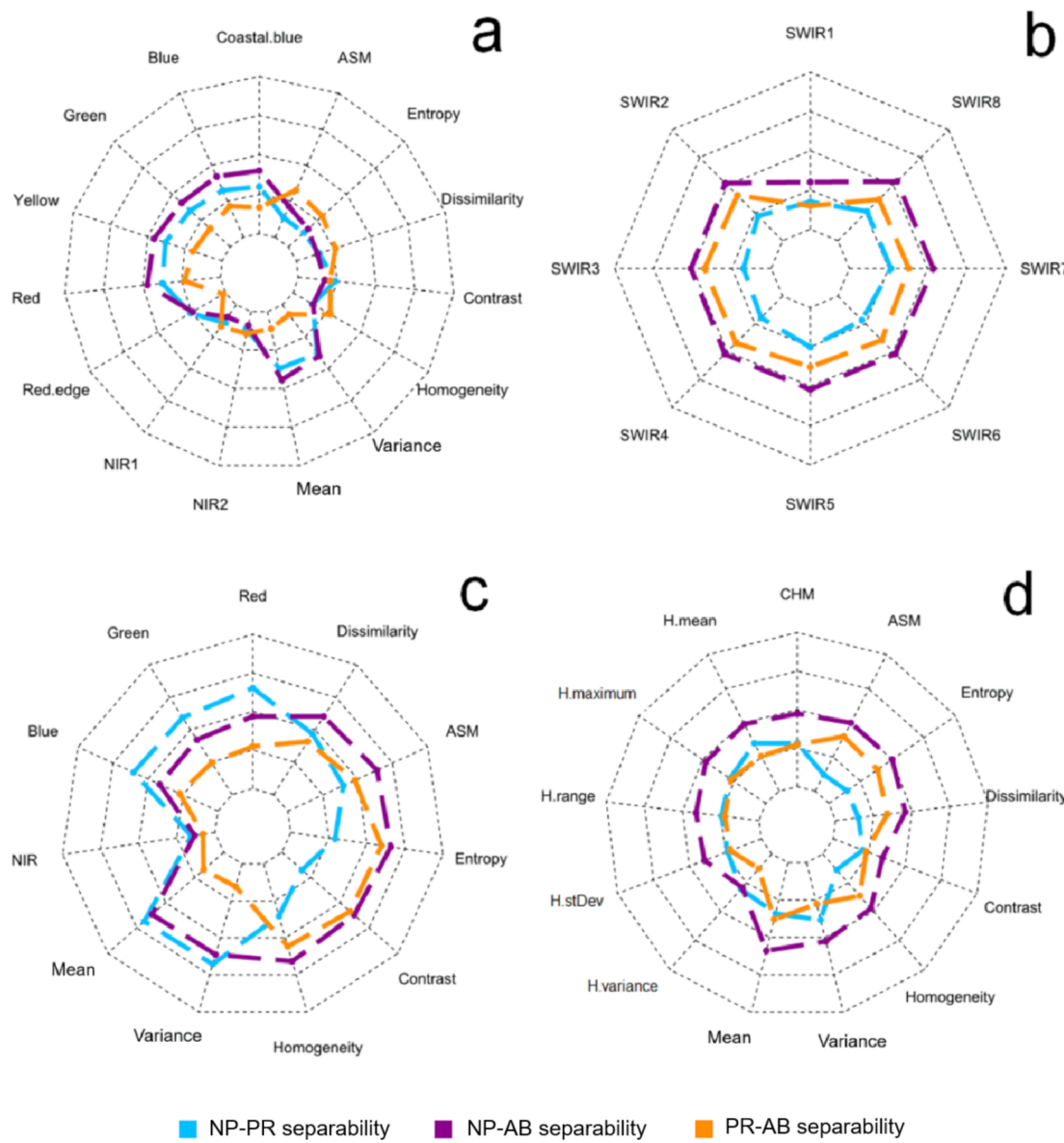


Fig. 7. Class separability produced by each descriptor according to the Jeffries-Matusita distance. a) WorldView-3 VNIR bands and GLCM features, b) WorldView-3 SWIR bands, c) Very High-Resolution Airborne Image bands and GLCM features. d) SfM point cloud altimetric and GLCM features. Jeffries-Matusita distance varies between 0 and $\sqrt{2}$, where 0 is null separability and $\sqrt{2}$ is maximum separability.

to vegetation and soil moisture. The abandoned parcels do not receive irrigation while in productive parcels the farmers irrigate their crops avoiding a water stress situation. This fact suggests that the separability between PR and AB parcels could be greater in the dry season where there is hardly any rainfall. These facts, encourage the study of ALA in evergreen crops through time-series of vegetation and moisture indices.

The VHRA image achieved an OA between 0.986 and 0.962 using the VNIR bands (R, G, B, NIR) and the GLCM texture features extracted from the NDVI. The VHRA image was the most accurate data source. However, these images have lower radiometric quality than WV-3. These images do not have surface reflectance products. In addition, the images are taken during photogrammetric flights carried out on different dates and therefore with different atmospheric conditions and different solar angles, even using different sensors every year. These characteristics make it difficult to create a spatially and temporally transferable model. However, the excellent results obtained allow a monitoring plan for citrus crops in the entire Valencian territory by using several locally trained models. Alternatively, the radiometric quality of the VHRA imagery could be enhanced by applying image fusion techniques (e.g.,

Wang and Atkinson, 2018; Houborg et al., 2018; Zhao et al., 2022) that allows fusion with Sentinel-2.

SfM point clouds achieved a lower performance than optical spectral data. SfM point clouds achieved an OA between 0.836 and 0.822 using altimetric features and GLCM texture features extracted from the CHM. Combining multispectral and altimetric data produced a slight improvement in model performance. However, generating 3D point clouds using SfM is computationally and operationally demanding, so it is not suitable for large areas. This fact may not justify the use of 3D point clouds generated by SfM for this problem. An alternative for large-scale studies would be to use Airborne Laser Scanning (ALS) data to extract texture features from the CHM. The classification performance obtained is promising and highlights the importance of texture features extracted from CHM for identifying spatial patterns of crops. This information could complement moderate-resolution imagery such as Sentinel-2, of free access, large coverage, and high temporal resolution when spatial planting patterns are a key feature. Texture features extracted from the CHM allowed to model citrus planting frames. However, we assume that there may be a CHM underestimation under

certain circumstances. The first is the DTM overestimation in the presence of dense vegetation. The second is the smoothing effect of the tree canopies produced by the SfM algorithm. Although the characteristics of citrus crops make it easy to obtain a consistent CHM, in other scenarios this can be a limiting factor. The use of ALS systems with higher penetration (even more for Full-Waveform LiDAR systems), could also be an alternative to compute a more accurate DTM. Another alternative is the use of the algorithm proposed by Tan et al. 2018 to remove misclassified ground points on vegetation using the spectral information of the images captured by the RPAS.

Including texture features produced improvements in all tested models, especially when they were computed from the NDVI. The descriptors relevance showed that texture features complement the spectral data and covers gaps where spectral information does not produce enough separability between classes. These results agree with our previous experiences (Morell-Monzo et al., 2021) and confirm the importance of texture features extracted from very high spatial resolution data to identify the status of evergreen crops (e.g., citrus crops). The importance of textures lies on their ability to model spatial planting patterns (planting frames) typical of fruit crops.

This work provides new research to identify the status of citrus crops and other evergreen crops at parcel level using remote sensing data. In particular, the work provides advances towards the operational implementation of checks by monitoring in the context of Common Agricultural Policy and the quantification of agricultural land abandonment in the Valencian Community region. One of the biggest challenges of remote sensing applications is to create accurate models that require little training data, reduce recalibration efforts, and that are spatially and temporally transferable. In the first steps of application of these products for monitoring the status of agricultural parcels, it is necessary to validate the models with more data and in other areas, since a lower performance is expected outside the study area and other dates. Future efforts should focus on quantifying the spatial-temporal transferability of the models. Furthermore, future research should clarify the optimal acquisition date of the images according to the rainfall and temperature regime.

5. Conclusions

This work assessed the potential of high-resolution spectral, SfM point clouds and textural descriptors to identify the status of citrus parcels in the Comunitat Valenciana region (Spain). Different analyzes involving combinations of WorldView-3, Very High-Resolution Airborne Imagery and RPAS-SfM point clouds data were carried out to assess the impact of combining the different data sources on classification accuracy. It was shown the high potential of WV-3 and VHRA imagery to identify citrus crops' status (greater than 0.900) from a single image. The SfM data showed a lower potential (≈ 0.825) by itself. Combining multispectral and 3D point clouds produced little improvement in the classification accuracy. The WV-3 SWIR bands showed a high potential to detect abandoned parcels as they produce more spectral separability over the productive parcels in the 1570 nm – 2330 nm spectrum. The results also show the importance of GLCM texture features extracted from sub-metric images due to their ability to model spatial planting patterns typical of fruit crops.

This work provides new research for the operational implementation of checks by monitoring and quantification of agricultural land abandonment in the CV region. The experience of this research can help the implementation of tools that enable monitoring the citrus crop status in other areas and other similar perennial crops. The research provided useful information on which sources of remotely sensed data are most effective for citrus crop status classification, either on its own or in combination. It also showed the performance of two machine learning algorithms: Random Forest and Support Vector Machines. This provides valuable information for selecting the appropriate combination of remotely sensed data sources and machine learning algorithms.

Funding

This research was funded by regional government of Spain, Generalitat Valenciana, within the framework of the research project AICO/2020/246. Funding for open access charge: CRUE-Universitat Politècnica de València.

CRediT authorship contribution statement

Sergio Morell-Monzo: Conceptualization, Methodology, Software, Validation, Formal analysis, Investigation, Data curation, Writing – original draft, Visualization. **Javier Estornell:** Conceptualization, Methodology, Investigation, Data curation, Resources, Writing – review & editing, Supervision, Project administration, Funding acquisition. **María-Teresa Sebastiá-Frasquet:** Conceptualization, Methodology, Investigation, Resources, Writing – review & editing, Supervision, Project administration.

Declaration of Competing Interest

The authors declare that they have no known competing financial interests or personal relationships that could have appeared to influence the work reported in this paper.

Data availability

Data will be made available on request.

References

- Alcántara, C., Kuemmerle, T., Prishchepov, A.V., Radloff, V.C., 2012. Mapping abandoned agriculture with multi-temporal MODIS satellite data. *Rem. Sens. Environ.* 124, 334–347. <https://doi.org/10.1016/j.rse.2012.05.019>.
- Breiman, L., 2001. Random forests. *Mach. Learn.* 45, 5–32. <https://doi.org/10.1023/A:101933404324>.
- Cortes, C., Vapnik, V., 1995. Support-vector networks. *Mach. Learn.* 20, 273–297. <https://doi.org/10.1007/BF00994018>.
- Czesak, B., Rózycka-Czas, R., Salata, T., Dixon-Gough, R., Hernik, J., 2021. Determining the intangible: detecting land abandonment at local scale. *Rem. Sens.* 13, 1166. <https://doi.org/10.3390/rs13061166>.
- Digital Globe, 2014. WorldView-3 data sheet. https://www.spaceimagingme.com/downloads/sensors/datasheets/DG_WorldView3_DS_2014.pdf.
- Estel, S., Kuemmerle, T., Alcántara, C., Levers, C., Prishchepov, A.V., Hostert, P., 2015. Mapping farmland abandonment and recultivation across Europe using MODIS NDVI time series. *Rem. Sens. Environ.* 163, 312–325. <https://doi.org/10.1016/j.rse.2015.03.028>.
- Generalitat Valenciana, 2021. Portal Estadístico de la Generalitat Valenciana. Fichas Municipales. Available online: <http://www.pegv.gva.es/es/fichas> (accessed on 05 December 2021).
- Grădinaru, S.R., Kienast, F., Psomas, A., 2019. Using multi-seasonal Landsat imagery for rapid identification of abandoned land in areas affected by urban sprawl. *Ecol. Indic.* 96, 79–86. <https://doi.org/10.1016/j.ecolind.2017.06.022>.
- Hall-Beyer, M., 2017. Practical guidelines for choosing GLCM textures to use in landscape classification tasks over a range of moderate spatial scales. *Int. J. Rem. Sens.* 38 (5), 1312–1338.
- Haralick, M.R., Shanmugam, K., Distein, I., 1973. Textural features for image classification. *IEEE Trans. Syst. Man Cybernet.* 3, 610–620. <https://doi.org/10.1109/TSMC.1973.4309314>.
- Houborg, R., McCabe, M.F., 2018. A cubesat enabled spatio-temporal enhancement method (CESTEM) utilizing planet, landsat and MODIS data. *Rem. Sens. Environ.* 209, 211–226. <https://doi.org/10.1016/j.rse.2018.02.067>.
- Institut Valencià d'Investigacions Agràries – IVIA. Citricultura valenciana. <http://gipcir.icos.ivia.es/citricultura-valenciana> (accessed on 20 October 2022).
- Karasik, N., Dejoux, J.-F., Montel, C., Sheeren, D., 2022. Spatial dependence between training and test sets: another pitfall of classification accuracy assessment in remote sensing. *Mach. Learn.* 111 (7), 2715–2740.
- Khosravipour, A., Skidmore, A.K., Isenburg, M., Wang, T., Hussin, Y.A., 2014. Generating pitfree canopy height models from airborne lidar. *Photogram. Eng. Rem. Sens.* 80 (9), 863–872. <https://doi.org/10.14358/PERS.80.9.863>.
- Kolecka, N., Kozak, J., Kaim, D., Dobosz, M., Ginzler, C., Psomas, A., 2015. Mapping secondary forest succession on abandoned agricultural land with LiDAR point clouds and terrestrial photography. *Rem. Sens.* 7 (7), 00–8322. <https://doi.org/10.3390/rs7070830>.
- Kosmas, C., Kairis, O., Karavitis, C., Acikalin, S., Alcalá, M., Alfama, P., Athlapheng, J., Barrera, J., Belgacem, A., Solé-Benet, A., Brito, J., Chaker, M., Chanda, R., Darkoh, M., Ermolaeva, O., Fassouli, V., Fernandez, F., Gokceoglu, C., Gonzalez, D., Gungor, H., Hessel, R., Khatteli, H., Khitrov, N., Kounalaki, A., Laouina, A., Magole, L., Medina, L., Mendoza, M., Mulale, K., Ocakoglu, F., Ouessar, M.,

- Ovalle, C., Perez, C., Perkins, J., Pozo, A., Prat, C., Ramos, A., Ramos, J., Riquelme, J., Ritsema, C., Romanenkov, V., Sebego, R., Sghaier, M., Silva, N., Sizemskaya, M., Sonmez, H., Taamallah, H., Tezcan, L., de Vente, J., Zagal, E., Zeiligher, A., Salvati, L., 2015. An exploratory analysis of land abandonment drivers in areas prone to desertification. *CATENA* 128, 252–261.
- Liaw, A., Wiener, M., 2002. Classification and regression by randomForest. *R News* 2 (3), 18–22. <https://cran.r-project.org/web/packages/randomForest/index.html>.
- Löw, F., Prishchepov, A.V., Waldner, F., Dubovyk, O., Akramkhanov, A., Biradar, C., Lamers, J.P.A., 2018. Mapping cropland abandonment in the Aral Sea Basin with MODIS time series. *Rem. Sens.* 10 (2), 159. <https://doi.org/10.3390/rs10020159>.
- Meyer, D., Dimitriadou, E., Hornik, K., Weihs, A., Leisch, F., 2021. e1071: Misc Functions of the Department of Statistics, Probability Theory Group (Formerly: E1071), TU Wien. R package version 1.7-9. <https://CRAN.R-project.org/package=e1071>.
- Ministerio de Agricultura, Pesca y Alimentación, 2021. ESYRCE: Encuesta Sobre Superficies y Rendimientos del año 2020; Ministerio de Agricultura, Pesca y Alimentación: Madrid, Spain. <https://www.mapa.gob.es/es/estadistica/temas/estadisticas-agrarias/agricultura/esyrce/>.
- Ministerio de Agricultura, Pesca y Alimentación, 2022. ESYRCE: Encuesta Sobre Superficies y Rendimientos del año 2021; Ministerio de Agricultura, Pesca y Alimentación: Madrid, Spain. <https://www.mapa.gob.es/es/estadistica/temas/estadisticas-agrarias/agricultura/esyrce/>.
- Morell-Monzo, S., Sebastiá-Frasquet, M.T., Estornell, J., 2021. Land use classification of VHR images for mapping small-sized abandoned citrus plots by using spectral and textual information. *Rem. Sens.* 13 (4), 681. <https://doi.org/10.3390/rs13040681>.
- Perpiñá-Castillo, C., Kavalov, B., Diogo, V., 2018. Agricultural Land Abandonment in the EU within 2015–2030; (Technical Report JRC113718). Brussels, Belgium, European Commission.
- Portalés-Julià, E., Campos-Taberner, M., García-Haro, F.J., Gilabert, M.A., 2021. Assessing the Sentinel-2 Capabilities to identify abandoned crops using deep learning. *Agronomy* 11 (4), 654. <https://doi.org/10.3390/agronomy11040654>.
- Prins, A.J., Van Niekerk, A., 2021. Crop type mapping using LiDAR, Sentinel-2 and aerial imagery with machine learning algorithms. *Geo-spatial Inform. Sci.* 24 (2), 215–227.
- Prishchepov, A.V., Radloff, V.C., Dubinin, M., Alcantara, C., 2012. The effect of Landsat ETM/ETM image acquisition dates on the detection of agricultural land abandonment in Eastern Europe. *Rem. Sens. Environ.* 126, 195–209. <https://doi.org/10.1016/j.rse.2012.08.017>.
- Prishchepov, A.V., Abandonment, A.L., Bibliographies, O., 2020. Agricultural Land Abandonment. Oxford Bibliographies. Environmental Science. Oxford University Press. <https://doi.org/10.1093/obo/9780199363445-0129>.
- Richter, R., Schläpfer, D., 2019. Atmospheric and Topographic Correction (ATCOR Theoretical Background Document), DLR report:DLR-IB 564-03/2019, pp 142. https://www.rese-apps.com/pdf/atcor_atbd.pdf.
- Richter, R., Schläpfer, D., Atmospheric/Topographic Correction for Satellite Imagery, DLR Report DLR-IB 565-01/2019, Wessling, Germany, pp 210. ATCOR-2/3 User Guide, Version 9.4.0, July 2021. https://www.rese-apps.com/pdf/atcor3_manual.pdf.
- Ruiz, L.A., Almonacid-Caballer, J., Crespo-Pereyra, P., Recio, J.A., Pardo-Pascual, J., Sánchez-García, E., 2020. Automated classification of crop types and condition in a Mediterranean area using fine-tuned convolutional neural network. *Int. Arch. Photogramm. Rem. Sens. Spatial Inform. Sci.* Volume XLIII-B3-2020.
- Saini, R., Ghosh, S.K., 2018. Crop classification on single date Sentinel-2 imagery using random forest and support vector machine. *Int. Arch. Photogramm. Rem. Sens. Spatial Inform.* Volume XLII-5.
- Sheykhouisa, M., Mahdianpari, M., Ghanbari, H., Mohammadimanesh, F., Ghamisi, P., Homayouni, S., 2020. Support vector machine versus random forest for remote sensing image classification: a meta-analysis and systematic review. *IEEE J. Sel. Top. Appl. Earth Observ. Rem. Sens.* 13, 6308–6325. <https://doi.org/10.1109/JSTARS2020.3026724>.
- Stock, A., 2022. Spatiotemporal distribution of labeled data can bias the validation and selection of supervised machine learning algorithms: a marine remote sensing example. *ISPRS J. Photogramm. Rem. Sens.* 187, 46–60. <https://doi.org/10.1016/j.isprsjprs.2022.02.023>.
- Strijker, D., 2005. Marginal lands in Europe - causes of decline. *Basic Appl. Ecol.* 6, 99–106. <https://doi.org/10.1016/j.baae.2005.01.001>.
- Subedi, R.Y., Kristiansen, P., Cacho, O., in press. Drivers and consequences of agricultural land abandonment and its reutilization pathways: a systematic review. *Environ. Devol.* <https://doi.org/10.1016/j.envdev.2021.100681>.
- Szostak, M., Hawrylo, P., Piela, D., 2017. Using of Sentinel-2 images for automation of the forest succession detection. *Eur. J. Rem. Sens.* 51, 142–149. <https://doi.org/10.1080/22797254.2017.1412272>.
- Tan, Y., Wang, S., Xu, B., Zhang, J., 2018. An improved progressive morphological filter for UAV-based photogrammetric point clouds in river bank monitoring. *ISPRS J. Photogramm. Rem. Sens.* 146, 421–429. <https://doi.org/10.1016/j.isprsjprs.2018.10.013>.
- Vajsová, B., Fasbender, D., Wirnhardt, C., Lemajic, S., Devos, W., 2020. Assessing spatial limits of Sentinel-2 data on arable crops in the context of checks by monitoring. *Rem. Sens.* 12, 2195. <https://doi.org/10.3390/rs12142195>.
- Volpi, I., Marchi, S., Petacchi, R., Hoxha, K., Guidotti, D., 2023. Detecting olive grove abandonment with Sentinel-2 and machine learning: The development of a web-based tool for land management. *Smart Agric. Technol.* 3, 100068 <https://doi.org/10.1016/j.atech.2022.100068>.
- Wadoux, A.-M.-J.-C., Heuvelink, G.B.M., de Bruin, S., Brus, D.J., 2021. Spatial cross-validation is not the right way to evaluate map accuracy. *Ecol. Model.* 457. <https://doi.org/10.1016/j.ecolmodel.2021.109692>.
- Wang, Q., Atkinson, P.M., 2018. Spatio-temporal fusion for daily Sentinel-2 images. *Rem. Sens. Environ.* 204, 31–42. <https://doi.org/10.1016/j.rse.2017.10.046>.
- Yin, H., Prishchepov, A.V., Kuemmerle, T., Bleyhl, B., Buchner, J., Radloff, V.C., 2018. Mapping agricultural land abandonment from spatial and temporal segmentation of Landsat time series. *Rem. Sens. Environ.* 210, 12–24. <https://doi.org/10.1016/j.rse.2018.02.050>.
- Zhang, K., Chen, S.C., Whitman, D., Shyu, M.L., Yan, J., Zhang, C., 2003. A progressive morphological filter for removing nonground measurements from airborne LiDAR data. *IEEE Trans. Geosci. Rem. Sens.* 41 (4), 872–882. <https://doi.org/10.1109/TGRS.2003.810682>.
- Zhao, Y., Liu, D., 2022. A robust and adaptive spatial-spectral fusion model for PlanetScope and Sentinel-2 imagery. *GISci. Rem. Sens.* 59, 520–546. <https://doi.org/10.1080/15481603.2022.2036054>.